

ORIGINAL ARTICLE

In situ anchoring of Co₉S₈ nanoparticles on N and S co-doped porous carbon tube as bifunctional oxygen electrocatalysts

Hai-xia Zhong^{1,2,4}, Kai Li^{1,4}, Qi Zhang¹, Jun Wang^{1,2}, Fan-lu Meng^{1,3}, Zhi-jian Wu¹, Jun-min Yan³ and Xin-bo Zhang¹

The development of cost-effective yet highly active and robust bifunctional electrocatalyst for oxygen evolution reaction (OER) and oxygen reduction reaction (ORR) has been at the forefront of research into regenerative fuel cells and metal–air batteries. Here we report Co₉S₈ nanoparticles grown *in situ* on nitrogen- and sulfur-doped porous carbon (Co₉S₈/NSPC) as a bifunctional catalyst for OER and ORR using poly(2-aminothiazole) as a novel all-in-one multifunctional precursor. Unexpectedly, Co₉S₈/NSPC exhibits a low OER overpotential, positive ORR half-wave potential, small potential gap and high durability, thus making it one of the best bifunctional OER and ORR catalysts. This may be attributed to the heteroatom doping, porous structure and synergistic effects of Co₉S₈ and NSPC, as confirmed by density functional theory calculations. More importantly, as a proof-of-concept application, the air electrode with Co₉S₈/NSPC9–45 endows the Zn–air battery with a low discharge/charge overpotential and good cycling stability.

NPG Asia Materials (2016) 8, e308; doi:10.1038/am.2016.132; published online 9 September 2016

INTRODUCTION

Due to the high power density, high energy conversion efficiency and lack of pollution, the use of regenerative fuel cells and metal–air batteries as clean and efficient energy conversion and storage technologies can, to a great extent, mitigate the worldwide energy and ecological crises caused by the immoderate consumption of fossil fuels.^{1–4} At the heart of these devices is oxygen electrochemistry, which includes both the oxygen evolution reaction (OER) and oxygen reduction reaction (ORR) and involves a four-electron transfer process that exposes the sluggish reaction kinetics, resulting in severe energy conversion losses.^{5–7} Although many efficient single functional OER or ORR catalysts have been achieved, the exploration of ideal bifunctional catalysts for OER and ORR is still highly challenging because active ORR catalysts usually exhibit poor OER performances and vice versa. In this context, Pt and Ir alloys or oxides still represent the most efficient OER and ORR catalysts.^{8–10} Nevertheless, challenges such as their high cost, scarcity and low stability still limit the large-scale commercialization of these devices. Therefore, the development of efficient and cost-effective bifunctional catalysts for OER and ORR is of great scientific and technological importance but is still very challenging.

Recently, transition metallic chalcogenides (TMCs), particularly cobalt chalcogenides (for example, CoSe₂ and CoS₂), have been proposed as potential OER and/or ORR electrocatalysts due to their earth abundance and environmentally friendly features and their high catalytic activity.^{11–15} However, the obtained bifunctional performances of TMC nanoparticles (NPs) are still far from satisfying because of the low electronic conductivity, easy aggregation of NPs and, in particular, the intrinsic lack of active sites driving both OER and ORR that will inevitably compromise the reaction kinetics and lead to inferior bifunctional catalytic activities. In this context, active TMC NPs can be considered for loading on conductive carbonaceous substrates (for example, graphene and carbon nanotubes).^{16,17} However, the required intimate contact cannot be guaranteed by the simple mixing of TMC NPs with conventional carbons because TMC NPs are easily detached from the substrates due to gas bubbling/evolution during the catalytic reaction process. In principle, *in situ* anchoring of active TMC NPs on heteroatom-doped porous carbons can be a good solution to this problem due to their high electron conductivity, porous structure for high flux of mass transportation and the extra active sites induced by heteroatom doping.^{1,18–20} Furthermore, the possible synergistic effects between TMC NPs and heteroatom-doped porous carbon may be collected to

¹State Key Laboratory of Rare Earth Resource Utilization, Changchun Institute of Applied Chemistry, Chinese Academy of Sciences, Changchun, PR China; ²University of Chinese Academy of Sciences, Beijing, PR China and ³Key Laboratory of Automobile Materials Ministry of Education and College of Materials Science and Engineering Jilin University, Changchun, PR China

⁴These authors contributed equally to this work.

Correspondence: Professor X-b Zhang, State Key Laboratory of Rare Earth Resource Utilization, Changchun Institute of Applied Chemistry, Chinese Academy of Sciences, 5625 Renmin Street, Changchun 130022, PR China.

E-mail: xbzhang@ciac.ac.cn

Received 5 February 2016; revised 7 May 2016; accepted 23 June 2016

markedly enhance the OER and ORR performance. Therefore, it is highly important to explore the hybrids of TMCs and heteroatom-doped carbons towards novel bifunctional catalysts for both the OER and ORR.

Herein, as a proof-of-concept experiment, we first develop a facile approach for the *in situ* anchoring of Co₉S₈ NPs on nitrogen and sulfur co-doped porous carbon (NSPC) as an efficient bifunctional catalyst for OER and ORR, in which water-soluble Na₂SO₄ nanowires are used as a template due to their low cost and ease of fabrication and removal, thus ensuring the porous structure of Co₉S₈/NSPC. Furthermore, poly(2-aminothiazole) (P-2AT) is selected as the all-in-one N- and S-containing precursor for synthesizing NSPC while simultaneously providing a sulfur source for the *in situ* formation of Co₉S₈ NPs on self-derived carbon under heat treatment, thus guaranteeing the intimate contact of Co₉S₈ and NSPC. Unexpectedly, the resultant Co₉S₈/NSPC shows high catalytic performance with a low OER overpotential, a positive ORR half-wave potential ($E_{1/2}$), long-term durability and high selectivity. Furthermore, as a proof-of-concept application, the assembled Zn–air battery when Co₉S₈/NSPC is used as an air electrode, exhibits low discharge/charge overpotential and good cyclic stability compared with state-of-the-art Pt/C and RuO₂, thus showing its long-term availability.

EXPERIMENTAL PROCEDURES

Synthesis of Na₂SO₄ nanowire

Na₂SO₄ nanowire was synthesized using the organic-solvent-induced crystallization method. In a typical experiment, Na₂SO₄ (0.14 g) and polyvinylpyrrolidone (PVP, 0.05 g) were first dissolved in water (4 ml). After mixing well with ethylene glycol (20 ml), the aqueous solution was dropped into 1,4-dioxane (50 ml) under vigorous stirring. The solution turned white immediately. After stirring at room temperature for 5 min, the products were collected by centrifugation, washed with 1,4-dioxane and dried at 80 °C.

Synthesis of P-2AT nanotube

Na₂SO₄ (0.1 g) was well dispersed in 1,4-dioxane (50 ml) by sonication. Subsequently, 2-aminothiazole (0.5 g) and benzoperoxide (BPO, 1.22 g) were dispersed into the above solution and were stirred continuously at 80 °C with a reflux condenser and nitrogen protect for 24 h. The product was obtained by filtering, washing with water and freeze-drying. P-2AT NPs were synthesized using the same procedures, except no Na₂SO₄ was added.

Synthesis of Co₉S₈/NSPC

CoCl₂·6H₂O (45 mg) and P-2AT nanotubes (0.1 g) were dispersed in water by sonication for 30 min and stirring at room temperature for 2 h. The composites were obtained by freeze-drying. Then, the brown powders were calcinated at 900 °C under an Ar atmosphere for 2 h. To investigate the impacts of the amounts of cobalt precursor and carbonization temperatures on the catalytic performance, samples with various amounts of cobalt precursors (15, 45 and 75 mg) and heating temperatures (800, 900 and 1000 °C) were also prepared and were designated as Co₉S₈/NSPC9–15, Co₉S₈/NSPC9–45, Co₉S₈/NSPC9–75, Co₉S₈/NSPC8–45 and Co₉S₈/NSPC10–45, respectively.

Electrochemical test

All electrochemical tests were conducted in a three-electrode cell in 0.1 M KOH electrolyte, wherein rotating disk electrode (RDE) or rotating ring disk electrode (RRDE), Ag/AgCl electrode and Pt mesh served as the working electrode, reference electrode and counter electrode, respectively. Before each test, RDE (5.0 mm in diameter) or RRDE (5.61 mm in diameter) was polished by alumina slurries (1 and 0.05 μm) and washed with water and ethanol by sonication. Catalysts (5 mg) were dispersed into 1 ml of ethanol and 50 μl of Nafion solution by sonication for 30 min. Then, 10 μl of the catalyst inks was drop-cast on RDE, giving a catalyst loading of 0.247 mg cm⁻². For the

chronoamperometric response measurement, catalyst inks were loaded on carbon papers.

For OER, cyclic voltammetry tests were conducted in an O₂-saturated 0.1 M KOH solution from 0 to 0.7 V, with a scan rate of 5 mV s⁻¹ and a rotating speed of 1600 r.p.m. The chronoamperometric response measurements were carried out at 0.6 V in O₂-saturated 0.1 M KOH solution, with the carbon paper supported by catalysts as the working electrode. During the chronoamperometric measurement, the generated gas was monitored by a gas burette. RRDE measurements were conducted in O₂-saturated 0.1 M KOH solution, with a scan rate of 5 mV s⁻¹ and a rotating speed of 1600 r.p.m., while the ring potential was held constant at 0.5 V. The impedance was tested by electrochemical impedance spectroscopy measurements with an alternating current voltage at a 10 mV amplitude in a frequency range from 100 kHz to 0.1 Hz at 0.55 V. For ORR, cyclic voltammetry tests were conducted in N₂- and O₂-saturated 0.1 M KOH solution from -1.0 to 0.2 V with a scan rate of 50 mV s⁻¹. RDE measurements were carried out in O₂-saturated 0.1 M KOH solution with a scan rate of 5 mV s⁻¹ and different rotating speeds (400–2025 r.p.m.). RRDE measurements were conducted in O₂-saturated 0.1 M KOH solution with a scan rate of 5 mV s⁻¹ and a rotating speed of 1600 r.p.m., and the ring potential was constant at 0.5 V. The accelerated durability tests were carried out using potential cycles from 0.6 to 1.0 V vs reversible hydrogen electrode with a sweep rate of 100 mV s⁻¹. For the crossover effect, the test was carried out by the chronoamperometric response at -0.45 V in O₂-saturated 0.1 M KOH solution with a rotating speed of 1600 r.p.m., with methanol (2%, v/v) added at ~15 min. The reference electrode was calibrated with respect to the reversible hydrogen electrode and all polarization curves were corrected for capacitance and corrected with 85% infrared compensation.

Fabrication and test of zinc–air batteries

Zn–air battery test was conducted in a home-made battery, with catalyst-coated carbon paper (1 cm²) and Zn plate used as the air electrode and anode, respectively. Typically, catalysts (5 mg) were dispersed into 1 ml of ethanol and 50 μl of Nafion solution by sonication for 30 min. Then, some amount of catalyst inks was drop-cast on the carbon paper, giving a catalyst loading of 1 mg cm⁻². The electrolyte was a 6 M KOH solution containing 0.2 M Zn (CH₃COO)₂. Batteries tests were carried out via *I*–*V* characterization. For the cycling test, the constant current technique was utilized, with one cycle consisting of one discharging step (10 mA cm⁻² for 5 min), followed by one charging step with the same current density.

RESULTS AND DISCUSSION

Characterizations of Co₉S₈/NSPC

Co₉S₈/NSPC synthesis is illustrated in Figures 1a–c. First, Na₂SO₄ nanowires are fabricated via organic-solvent-induced recrystallization. Scanning electron microscopy (Figure 1d) confirms the nanowire morphology with a diameter of ~150 nm. The X-ray diffraction pattern reveals the orthorhombic structure of Na₂SO₄ (Supplementary Figure S1). Subsequently, P-2AT is successfully coated on the Na₂SO₄ nanowire by the oxidative-polymerization of 2-aminothiazole, as identified by the emergence of the broad N–H band of P-2AT (3295 cm⁻¹) and the shift of the C=N band (1619–1605 cm⁻¹) in Fourier transform infrared spectrum (Supplementary Figure S2).²¹ After removing Na₂SO₄ with simple water washing, the tubular P-2AT with diameter of ~270 nm is observed in the scanning electron microscopy image (Figure 1e), as verified by transmission electron microscopy (Figure 1f). The wall thickness is measured to be ~40 nm. After mixing with cobalt salts, they are directly converted to Co₉S₈/NSPCX–Y (X=8, 9 and 10, and Y=15, 45 and 75) via heat treatment in inert atmosphere, where X and Y represent the pyrolysis temperature and cobalt precursor content, respectively (Supplementary Figures S3–5). The Co₉S₈ particles (~50 nm in size) have a cubic structure and are dispersed on both the internal and external surfaces of NSPC tubes for Co₉S₈/NSPC9–45 (Supplementary

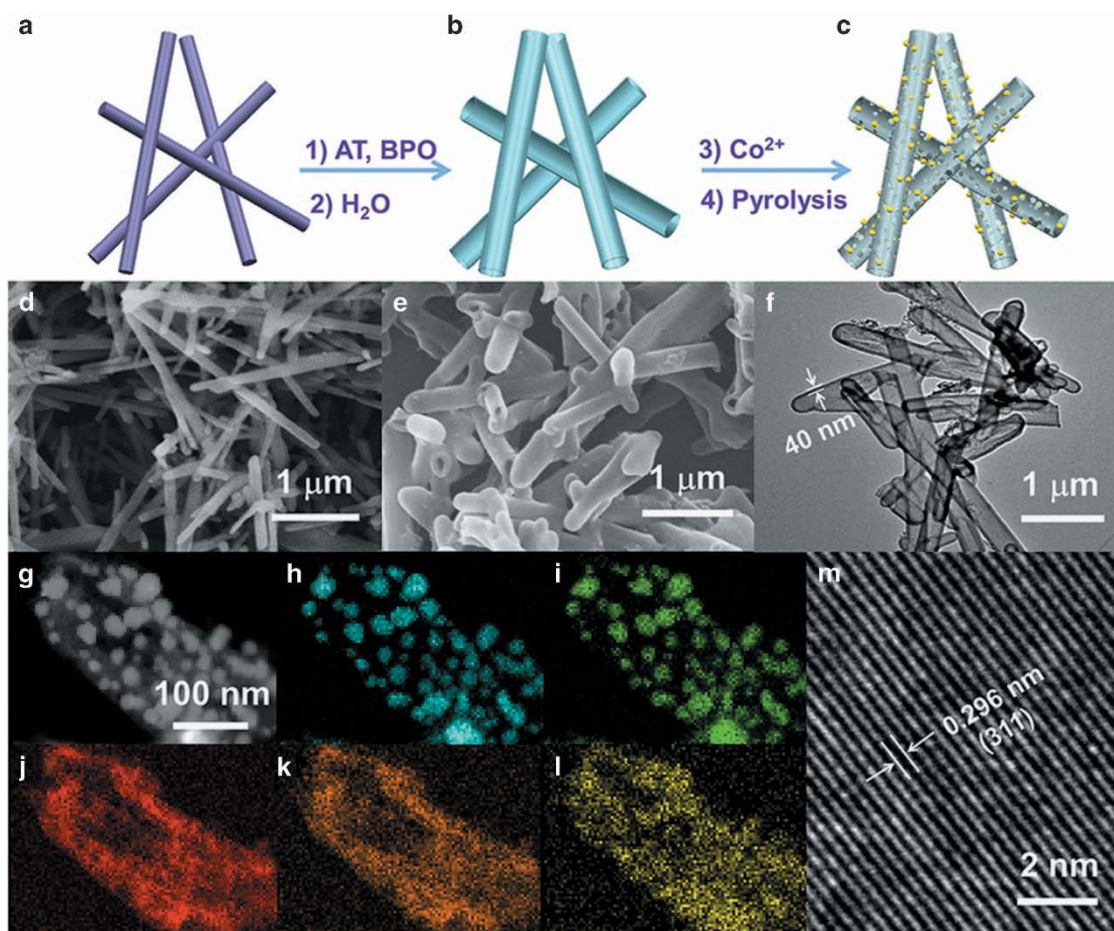


Figure 1 Schematic images of Na₂SO₄ (a), P-2AT (b) and Co₉S₈/NSPC (c); scanning electron microscopy images of Na₂SO₄ (d) and P-2AT (e); transmission electron microscopy (TEM) image of P-2AT (f); scan TEM image of Co₉S₈/NSPC9-45 (g); the corresponding element mapping images of Co (h), S (i), C (j), N (k) and O (l); and high-resolution TEM image of Co₉S₈/NSPC9-45 (m).

Figures S7c, S9 and S10).²² Moreover, the shrinkage and erosion of P-2AT at high temperature cause a decrease in the tube diameter and thickness and even partly broken tubes. Notably, the particle size of Co₉S₈ and the extent of broken tubes increase with the increased amounts of cobalt precursors and higher pyrolysis temperature (Supplementary Figures S7). The scan transmission electron microscopy image of Co₉S₈/NSPC9-45 further shows the tube morphology decorated with uneven Co₉S₈ particles (Figure 1g). Accordingly, the element mapping images show that Co and S overlay the particles, whereas C, N and O are homogeneously distributed on the entire structure (Figures 1h–l). In addition, S is partially distributed on the tube, thus indicating the incorporation of S in the carbon matrix, which is quite different from that of NSPC due to the growth of Co₉S₈ particles (Supplementary Figure S13). Furthermore, the well-defined lattice fringe of the particles is indexed to the (311) plane of cubic Co₉S₈ structure, in agreement with the X-ray diffraction results (Figure 1m; Supplementary Figures S10 and S14).

The Brunauer–Emmett–Teller (BET) surface areas and pore structures of the as-prepared materials were also investigated by N₂ adsorption–desorption measurements (Supplementary Figure S15; Supplementary Table S1). The pore distribution of Co₉S₈/NSPC9-45 indicates the coexistence of mesopores and macropores analyzed by the Barrett–Joyner–Halenda method, which are in favor of mass transfer.^{23,24} Comparatively, Co₉S₈/NSPC9-15 gains a higher BET surface area (317 m² g^{−1}) than Co₉S₈/NSPC9-45 (281 m² g^{−1}) and

Co₉S₈/NSPC9-75 (196 m² g^{−1}) due to its lower Co content and smaller Co₉S₈ particles (Supplementary Figures S8 and S9). In addition, with the same amount of Co precursors, the BET surface area of Co₉S₈/NSPC9-45 is higher than those of Co₉S₈/NSPC8-45 (184 m² g^{−1}) and Co₉S₈/NSPC10-45 (234 m² g^{−1}). This phenomenon is ascribed to insufficient or excessive carbon corrosion, and smaller or larger Co₉S₈ particles at, respectively, a low or high pyrolysis temperature (Supplementary Figures S16 and 17). Another control sample with Co₉S₈ on nitrogen- and sulfur-doped carbon (Co₉S₈/NSC; Supplementary Figures S11 and 12) shows an extremely low BET surface area (24 m² g^{−1}). Overall, the key factors of the Co precursor content, pyrolysis temperature and nanowire template determine the high surface area of Co₉S₈/NSPC9-45 that will influence the electrocatalytic performance (vide infra).

X-ray photoelectron spectroscopy is applied to probe the chemical structure of these samples (Figure 2; Supplementary Figures S18; Supplementary Table S2). The high-resolution C1s spectrum is deconvoluted into several peaks, corresponding to C–S–C (284.0 eV), C=C–C (284.7 eV), C–O (285.2 eV), C–N (286.2 eV) and O=C–OH (288.6 eV),^{25,26} thus revealing the successful doping of N and S in the carbon matrix. In addition, the peaks that are assigned to O=C–OH gradually become unclear due to the instability of oxygen species at higher temperatures. For N1s peaks, three components are obtained: pyridinic-N (N1, 398.5 eV), pyrrolic-N (N2, 399.6 eV) and graphitic-N (N3, 401.1 eV).^{27–29} Furthermore, the

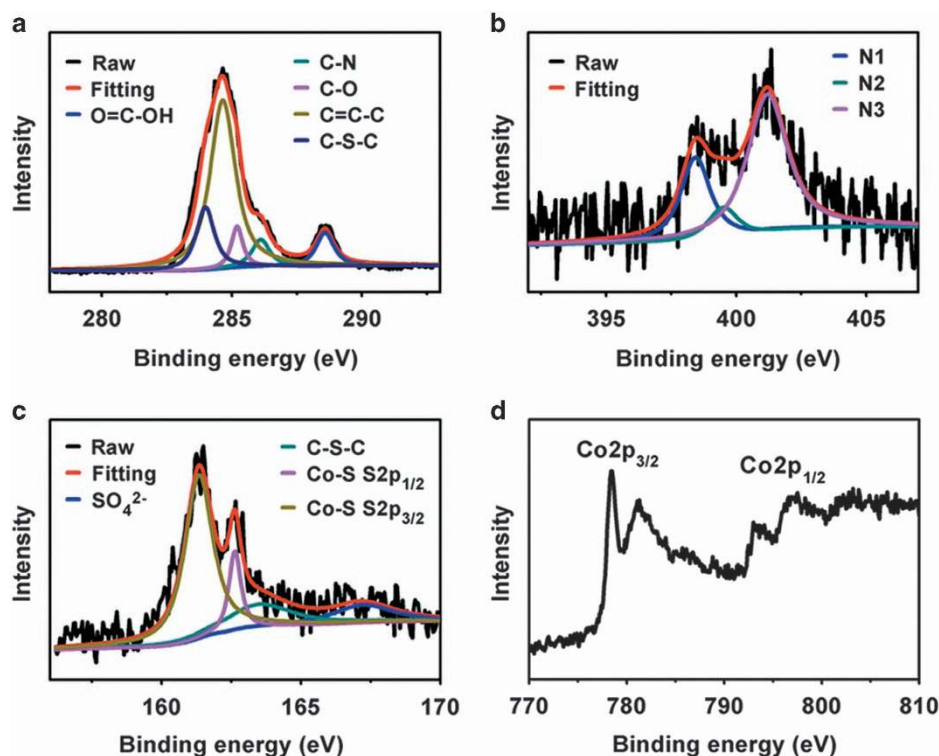


Figure 2 High-resolution C1s (a), N1s (b), S2p (c) and Co2p (d) X-ray photoelectron spectroscopy spectra of Co₉S₈/NSPC9-45.

relative fractions of N1 and N2 decrease with the increasing heating temperature because of their instabilities at high temperatures. Therefore, N1 and N3 peaks of Co₉S₈/NSPC9-45 predominantly account for the enhanced OER and ORR performances.^{20,28,29} Furthermore, S2p peaks are deconvoluted into four S contributions: the peaks at 161.5 and 162.9 eV are assigned to S2p_{3/2} and S2p_{1/2} in Co-S, respectively, and the peaks at 164.1 and 167.7 eV are due to C-S-C and SO₄²⁻, respectively^{22,25,27}, thus confirming the presence of S doping and Co-S composites, consistent with the element mapping results. It is worth noting that the relative ratio of C-S-C and Co-S is decreased with an increase in pyrolysis temperature because of the gradual forming of Co₉S₈ (Supplementary Figure S6d). The core-level spectrum of Co is divided into two main signals assigned to Co2p_{1/2} and Co2p_{3/2}, and the spin-orbit doublets confirm the presence of Co²⁺ and Co³⁺.³⁰⁻³² Hence, both Co₉S₈ and NSPC are expected to act as potential active sites for OER and ORR.

Electrochemical performance for ORR and OER

The OER electrocatalytic activities of Co₉S₈/NSPC are first evaluated using a three-electrode system. For comparison, the electrochemical performances of the physical mixtures of NSPC and Co₉S₈ (Co₉S₈+NSPC), and Pt/C and RuO₂ are also tested. Both Co₉S₈ and NSPC exhibit high overpotentials (10 mA cm⁻²) of 0.41 and 0.61 V, respectively, which may be due to the low conductivity of Co₉S₈ and the intrinsic low catalytic activity of NSPC (Figure 3a). Improved performance is achieved by Co₉S₈+NSPC, although its decreased overpotential (0.37 V) is still far from satisfactory. By contrast, Co₉S₈/NSPC9-45 obtains superior activity (0.31 V) associated with its low charge transfer impedance (Supplementary Figures S23 and 24), thus validating the synergistic effect between Co₉S₈ and NSPC. For Co₉S₈/NSC, the low BET surface area and less porous structure result in fewer active sites and oxygen transfer channels, and thus, a

larger overpotential (0.38 V, Figure 3a). Although it has a higher BET surface area, Co₉S₈/NSPC9-15 exhibits slightly lower catalytic activity compared with Co₉S₈/NSPC9-45 because it contains a smaller amount of Co₉S₈ particles (Supplementary Figure S25). Furthermore, the high OER behavior of Co₉S₈/NSPC9-45 is deduced from its lowest Tafel slope (68 mV dec⁻¹) among the prepared samples, which is even comparable to that of RuO₂ (50 mV dec⁻¹), thus indicating its more favorable kinetics (Figure 3b; Supplementary Table S3).³³⁻³⁵ Moreover, scarcely any yield of peroxide is monitored by RRDE technique, revealing a 4e⁻ OER process at the Co₉S₈/NSPC9-45 electrode (Supplementary Figure S26a). The agreement of the theoretical and experimental oxygen productions shows that the Faradaic efficiency at Co₉S₈/NSPC9-45 electrode is ~100% (Supplementary Figure S26b).

To explore the ORR electrocatalytic activity, RDE measurements were performed.^{1,10} Similarly, a high electrical resistance of Co₉S₈ leads to its low ORR catalytic activity, with a negative $E_{1/2}$ (0.5 V, Figure 3c). Although NSPC shows high conductivity, it is still plagued by inferior $E_{1/2}$ (0.62 V) due to the insufficient active sites. Exploiting the advantages of NSPC and Co₉S₈, a more positive $E_{1/2}$ (0.68 V) is achieved by Co₉S₈+NSPC, although this value is not satisfactory. In contrast, the intimate contact between NSPC and Co₉S₈ of Co₉S₈/NSPC9-45 hybrid results in faster charge transfer and a significantly improved ORR performance, with an $E_{1/2}$ of 0.79 V, thus indicating the synergistic catalytic activity of Co₉S₈ and NSPC (Figure 3c; Supplementary Figure S27). In addition, Co₉S₈/NSC, which possesses smaller Co₉S₈ particles, shows a lower $E_{1/2}$ (0.72 V), revealing that the ORR performance is governed by the BET surface area and various pores in addition to the particle size of active species. However, Co₉S₈/NSPC9-15 with the highest BET surface area exhibits a slightly lower ORR performance compared with the Co₉S₈/NSPC9-45 due to the smaller number of Co₉S₈ particles, thus

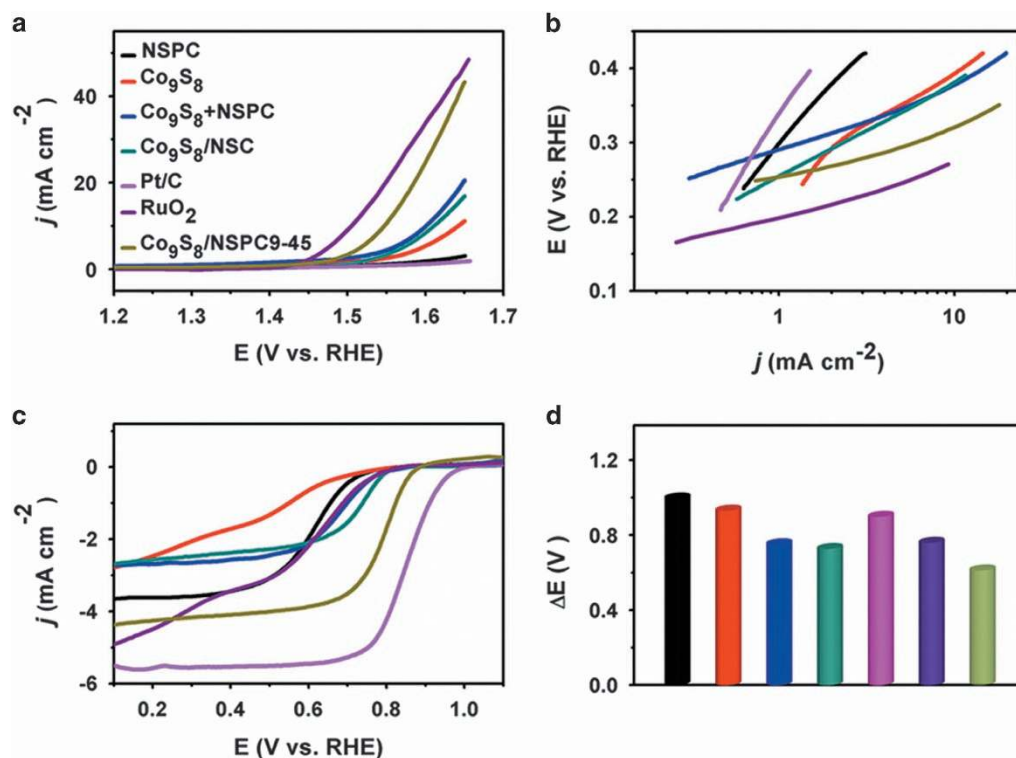


Figure 3 OER polarization curves (a), Tafel plots (b) and ORR polarization curves (c) and potential gaps (ΔE , d) of NSPC, Co₉S₈, Co₉S₈+NSPC, Co₉S₈/NSC, Pt/C, RuO₂ and Co₉S₈/NSPC9-45.

clarifying the greater importance of the intrinsic active sites for controlling the ORR performance.

To better understand the ORR mechanism, the kinetic parameters are analyzed using the Koutecký–Levich equation. The good linearity of the Koutecký–Levich plots and nearly parallel fitted lines for Co₉S₈/NSPC9-45 suggests a first-order reaction towards oxygen and similar electron transfer number at various potentials (Supplementary Figure S28).^{2,36,37} The electron number (n) of Co₉S₈/NSPC9-45 is calculated to be 3.94 (0.3 V), similar to that of Pt/C (3.96), which indicates that it favors a 4e⁻ oxygen reduction process. However, Co₉S₈, NSPC, Co₉S₈+NSPC and Co₉S₈/NSC show a coexistence of 2e⁻ and 4e⁻ oxygen reduction processes, with n values of 2.8, 3.38, 3.03 and 3.14, respectively, thus further highlighting the superior ORR catalytic activity of Co₉S₈/NSPC9-45 (Supplementary Figure S29; Supplementary Table S3). Moreover, the peroxide (HO₂⁻) yield was detected by the RRDE technique to further understand the electron transfer pathway (Supplementary Figure S30). Remarkably, the HO₂⁻ yield of Co₉S₈/NSPC9-45 is <10% at the 0–0.65 V potential range, giving an n of 3.83–3.96, consistent with the results based on the RDE data. Nevertheless, NSPC, Co₉S₈, Co₉S₈+NSPC and Co₉S₈/NSC show a coexistence of 2e⁻ and 4e⁻ oxygen reduction pathways, with average HO₂⁻ yields of 21%, 49%, 33% and 37%, respectively, indicating that the *in situ* growth of Co₉S₈ on NSPC is an effective approach for improving the electrocatalytic performance for ORR. In addition, its Tafel slope at a small current density is similar to that of Pt/C, suggesting that the transfer of the first electron is the rate determining step at the Co₉S₈/NSPC9-45 electrode (Supplementary Figure S31). We note that the Co₉S₈/NSPC9-45 and NSPC show higher OER and ORR performances than the porous carbon tube, indicating the significant roles of Co₉S₈ growth and the doping of heteroatoms in

the improvement of catalytic activity (Supplementary Figure S32; Supplementary Table S3).³⁸

The potential gap between OER (E at 10 mA cm⁻²) and ORR ($E_{1/2}$) is a key parameter of bifunctional electrocatalysts and is evaluated here.^{1,4,5,35,39} As expected, Co₉S₈/NSPC9-45 with the minimum ΔE (0.75 V) has an obvious advantage over Co₉S₈ (1.14 V), NSPC (1.22 V), Co₉S₈+NSPC (0.92 V) and Co₉S₈/NSC (0.89 V) and even surpasses Pt/C (1.1 V) and RuO₂ (0.93 V; Figure 3d; Supplementary Table S3). Moreover, compared with the previously reported catalysts with bifunctionality for OER and ORR, the performance of Co₉S₈/NSPC9-45 can be ranked at the highest level (Supplementary Table S4).

The durability of Co₉S₈/NSPC9-45 is further assessed by cyclic voltammetry and chronoamperometric measurements. Either 5000 OER potential cycles or 10 h of continuous chronoamperometric tests of Co₉S₈/NSPC9-45 cause only a slight degradation in its current, indicating its long-term durability during the OER process (Supplementary Figures S33 and S34). During the ORR process, a smaller negative shift of $E_{1/2}$ and smaller loss in the ORR current of Co₉S₈/NSPC9-45 are observed after 5000 potential cycles and 8 h chronoamperometric test. However, Pt/C suffers more loss in $E_{1/2}$ and current under identical conditions, suggesting the superior ORR durability of Co₉S₈/NSPC9-45. When injecting methanol, the chronoamperometric response of Co₉S₈/NSPC9-45 exhibits little change and immediately recovers, whereas Pt/C exhibits a distinct and unrecoverable drop in ORR current, thus revealing the higher selectivity of Co₉S₈/NSPC9-45 with methanol tolerance.

To gain further insights into the mechanisms of ORR and OER of Co₉S₈/NSPC, density functional theory calculations were conducted by using the Vienna *ab initio* simulation package (Supplementary Figures S35). The Gibbs free energy diagrams of ORR and OER of

Co₉S₈/SN supports (Co₉S₈/SN-C1 and Co₉S₈/SN-C2) are calculated to further elucidate the reaction processes (Figure 4; Supplementary Figure S39). All of the elementary reactions of ORR and OER are

exothermic/endothermic when the potential reaches $-0.131/0.930$ V vs normal hydrogen electrode, thus confirming the feasibility of the OER and ORR reactions with Co₉S₈/SN supports as electrocatalysts.

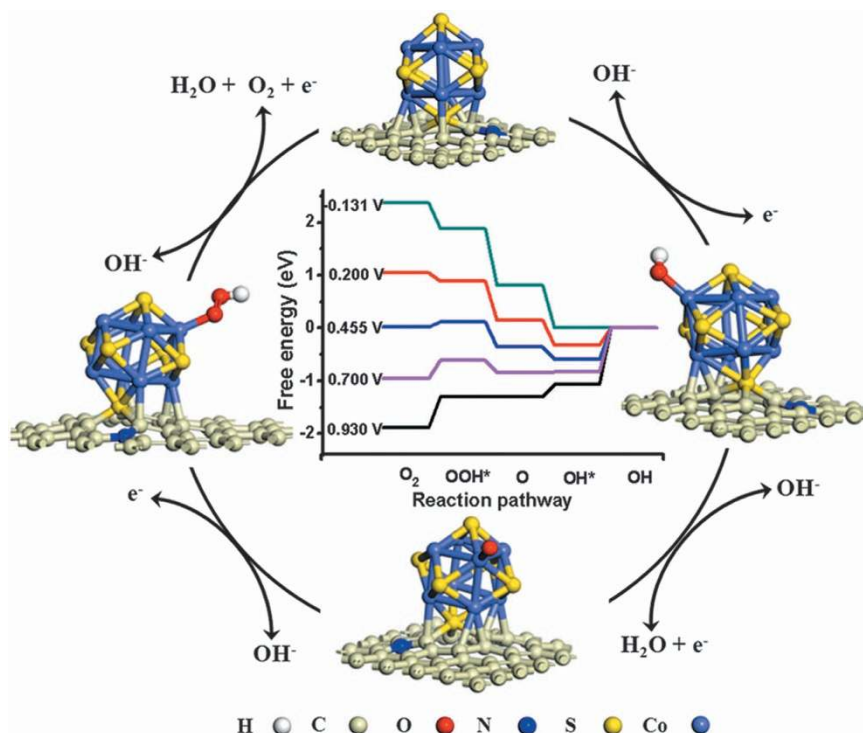


Figure 4 Free energy diagram of the Co₉S₈/SN-C2 at different applied potentials and the corresponding reaction mechanism of OER and ORR.

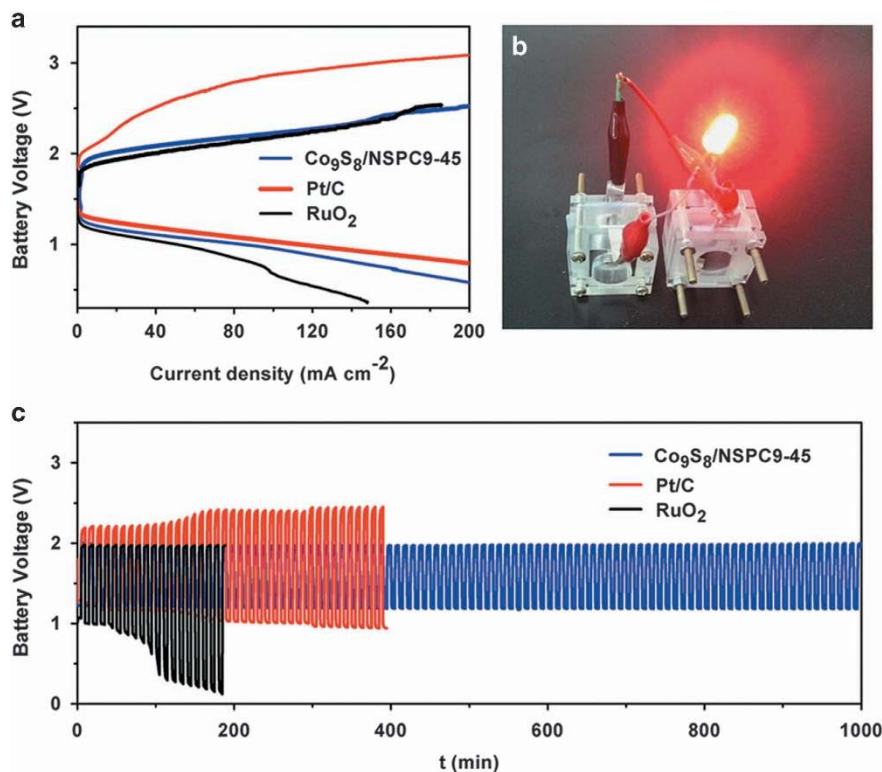


Figure 5 (a) Charge and discharge polarization curves of Zn-air batteries with Pt/C, RuO₂ and Co₉S₈/NSPC9-45 as air electrodes; (b) photograph of light-emitting diode driven by the two Zn-air batteries pack with Co₉S₈/NSPC9-45 as air electrode; (c) charge and discharge cycling curves of Zn-air batteries with Pt/C, RuO₂ and Co₉S₈/NSPC9-45 as air electrodes.

Moreover, the corresponding ORR and OER overpotentials for Co₉S₈/SN-C2 are 0.586 and 0.475 V, respectively, with respect to the equilibrium potential and are 0.586 and 0.827 V, respectively, for Co₉S₈/SN-C1, thus demonstrating that Co₉S₈/SN-C2 is superior to Co₉S₈/SN-C1 as a bifunctional catalyst and can improve the performance of both ORR and OER. In addition, it is worth noting that a slightly discrepancy will exist between the calculated and measured results because several experimental effects (for example, pH, active surface area and particle size) are difficult to consider in the calculation.⁴⁰

Performance of rechargeable Zn–air battery

Inspired by the superior electrochemical performances described above and to evaluate the bifunctional catalytic performance in practical devices, a rechargeable Zn–air battery with Co₉S₈/NSPC9–45 as the air electrode was further assembled. It is worth noting that the battery is tested in ambient conditions using atmospheric air instead of pure oxygen. To our surprise, such a battery shows the discharge and charge voltage of 1.07 and 2.11 V at the current density of 50 mA cm⁻², similar to a discharge voltage of Pt/C (1.15 V) and a charge voltage of RuO₂ (2.05 V) at the same current density, respectively (Figure 5a), thus demonstrating catalytic activities comparable to those of the benchmark ORR and OER catalysts. More importantly, it outperforms them with the charge voltage of Pt/C (2.60 V) and discharge voltage of RuO₂ (0.99 V). Only slight changes in the voltages are observed after 100 charge and discharge cycles. In contrast, the discharge voltage for RuO₂ is markedly reduced after 10 cycles, and the charge voltages of Pt/C increase continually starting at the beginning of the test, thus confirming the superior stability of Co₉S₈/NSPC9–45 (Figure 5c). Moreover, two Zn–air batteries can power a light-emitting diode and keep it shining for several weeks (Figure 5b). Therefore, Co₉S₈/NSPC9–45 armed with superior bifunctional catalytic activities and stabilities will be a competitive bifunctional catalyst for practical applications.

CONCLUSION

In conclusion, we first developed a facile and efficient strategy for the synthesis of Co₉S₈/NSPC as an efficient bifunctional catalyst for OER and ORR. The *in situ* nucleation and growth of Co₉S₈ on NSPC guarantee the highly desired intimate coupling of these materials, strengthen the charge transfer and thus improve the catalytic performance. Unexpectedly, the Co₉S₈/NSPC exhibits high dual electrocatalytic activity, with a positive $E_{1/2}$ and an n close to 4 for ORR and a low OER overpotential, comparable to those of commercial Pt/C and RuO₂. More importantly, a low charge/discharge overpotential of Zn–air batteries is obtained when Co₉S₈/NSPC is used as the air electrode. In addition to its application as a powerful bifunctional catalyst for regenerative fuel cells and metal–air batteries, Co₉S₈/NSPC can be used in other fields, such as lithium–ion batteries and supercapacitors.

CONFLICT OF INTEREST

The authors declare no conflict of interest.

ACKNOWLEDGEMENTS

This work is financially supported by National Program on Key Basic Research Project of China (973 Program, grant no. 2012CB215500).

- 1 Zhao, A., Masa, J., Xia, W., Maljusch, A., Willinger, M. G., Clavel, G., Xie, K., Schlögl, R., Schuhmann, W. & Muhler, M. Spinel Mn-Co oxide in N-doped carbon nanotubes as a bifunctional electrocatalyst synthesized by oxidative cutting. *J. Am. Chem. Soc.* **136**, 7551–7554 (2014).
- 2 Liang, Y., Li, Y., Wang, H., Zhou, J., Wang, J., Regier, T. & Dai, H. Co₃O₄ nanocrystals on graphene as a synergistic catalyst for oxygen reduction reaction. *Nat. Mater.* **10**, 780–786 (2011).
- 3 Hu, Y., Zhang, T., Cheng, F., Zhao, Q., Han, X. & Chen, J. Recycling application of Li-MnO₂ batteries as rechargeable lithium-air batteries. *Angew. Chem. Int. Ed.* **54**, 4338–4343 (2015).
- 4 Ma, T. Y., Ran, J., Dai, S., Jaroniec, M. & Qiao, S. Z. Phosphorus-doped graphitic carbon nitrides grown *in situ* on carbon-fiber paper: flexible and reversible oxygen electrodes. *Angew. Chem. Int. Ed.* **54**, 4646–4650 (2015).
- 5 Zhao, Y., Kamiya, K., Hashimoto, K. & Nakanishi, S. Efficient bifunctional Fe/C/N electrocatalysts for oxygen reduction and evolution reaction. *J. Phys. Chem. C* **119**, 2583–2588 (2015).
- 6 Li, C., Han, X., Cheng, F., Hu, Y., Chen, C. & Chen, J. Phase and composition controllable synthesis of cobalt manganese spinel nanoparticles towards efficient oxygen electrocatalysis. *Nat. Commun.* **6**, 7345 (2015).
- 7 Gong, M., Li, Y., Wang, H., Liang, Y., Wu, J. Z., Zhou, J., Wang, J., Regier, T., Wei, F. & Dai, H. An advanced Ni-Fe layered double hydroxide electrocatalyst for water oxidation. *J. Am. Chem. Soc.* **135**, 8452–8455 (2013).
- 8 Lu, Y. C., Xu, Z. C., Gasteiger, H. A., Chen, S., Hamad-Schifferli, K. & Shao-Horn, Y. Platinum-gold nanoparticles: a highly active bifunctional electrocatalyst for rechargeable lithium-air batteries. *J. Am. Chem. Soc.* **132**, 12170–12171 (2010).
- 9 Antolini, E. Iridium as catalyst and cocatalyst for oxygen evolution/reduction in acidic polymer electrolyte membrane electrolyzers and fuel cells. *ACS Catal.* **4**, 1426–1440 (2014).
- 10 Cheng, N., Banis, M., Liu, J., Riese, A., Li, X., Li, R., Ye, S., Knights, S. & Sun, X. Extremely stable platinum nanoparticles encapsulated in zirconia nanocages by area-selective atomic layer deposition for oxygen reduction reaction. *Adv. Mater.* **27**, 277–281 (2014).
- 11 Gao, M. R., Gao, Q., Jiang, J., Cui, C. H., Yao, W. T. & Yu, S. H. A methanol-tolerant Pt/CoSe₂ nanobelt cathode catalyst for direct methanol fuel cells. *Angew. Chem. Int. Ed.* **50**, 4905–4908 (2011).
- 12 Tan, C. & Zhang, H. Two-dimensional transition metal dichalcogenide nanosheet-based composites. *Chem. Soc. Rev.* **44**, 2713–2731 (2015).
- 13 Liu, Y., Cheng, H., Lyu, M., Fan, S., Liu, Q., Zhang, W., Zhi, Y., Wang, C., Xiao, C., Wei, S., Ye, B. & Xie, Y. Low overpotential in vacancy-rich ultrathin CoSe₂ nanosheets for water oxidation. *J. Am. Chem. Soc.* **136**, 15670–15675 (2014).
- 14 Ganesan, P., Prabhu, M., Sanetuntikul, J. & Shanmugam, S. Cobalt sulfide nanoparticles grown on nitrogen and sulfur codoped graphene oxide: An efficient electrocatalyst for oxygen reduction and evolution reactions. *ACS Catal.* **5**, 3625–3637 (2015).
- 15 Wu, G., Chung, H. T., Nelson, M., Artyushkova, K., More, K. L., Johnston, C. M. & Zelenay, P. Graphene-enriched Co₉S₈-N-C non-precious metal catalyst for oxygen reduction in alkaline media. *ECS Trans.* **41**, 1709–1717 (2011).
- 16 Liang, Y., Wang, H., Diao, P., Chang, W., Hong, G., Li, Y., Gong, M., Xie, L., Zhou, J., Wang, J., Regier, T. Z., Wei, F. & Dai, H. Oxygen reduction electrocatalyst based on strongly coupled cobalt oxide nanocrystals and carbon nanotubes. *J. Am. Chem. Soc.* **134**, 15849–15857 (2012).
- 17 Wang, H., Liang, Y., Li, Y. & Dai, H. Co_{1-x}S-graphene hybrid: a high-performance metal chalcogenide electrocatalyst for oxygen reduction. *Angew. Chem. Int. Ed.* **50**, 10969–10972 (2011).
- 18 Duan, J., Chen, S., Dai, S. & Qiao, S. Z. Shape control of Mn₃O₄ nanoparticles on nitrogen-doped graphene for enhanced oxygen reduction activity. *Adv. Funct. Mater.* **24**, 2072–2078 (2014).
- 19 Wei, W., Liang, H., Parvez, K., Zhuang, X., Feng, X. & Müllen, K. Nitrogen-doped carbon nanosheets with size-defined mesopores as highly efficient metal-free catalyst for the oxygen reduction reaction. *Angew. Chem. Int. Ed.* **53**, 1570–1574 (2014).
- 20 Zhao, Y., Nakamura, R., Kamiya, K., Nakanishi, S. & Hashimoto, K. Nitrogen-doped carbon nanomaterials as non-metal electrocatalysts for water oxidation. *Nat. Commun.* **4**, 2390 (2013).
- 21 Yildirim, M. & Kaya, I. A comparative study of aminothiazole-based polymers synthesized by chemical oxidative polymerization. *Synth. Met.* **162**, 436 (2012).
- 22 Feng, L. L., Li, G. D., Liu, Y., Wu, Y., Chen, H., Wang, Y., Zou, Y. C., Wang, D. & Zou, X. Carbon-armored Co₉S₈ nanoparticles as all-pH efficient and durable H₂-evolving electrocatalysts. *ACS Appl. Mater. Interfaces* **7**, 980–988 (2015).
- 23 Liang, J., Jiao, Y., Jaroniec, M. & Qiao, S. Z. Sulfur and nitrogen dual-doped mesoporous graphene electrocatalyst for oxygen reduction with synergistically enhanced performance. *Angew. Chem. Int. Ed.* **51**, 11496–11500 (2012).
- 24 Liang, H. W., Wei, W., Wu, Z. S., Feng, X. & Müllen, K. Mesoporous metal-nitrogen-doped carbon electrocatalysts for highly efficient oxygen reduction reaction. *J. Am. Chem. Soc.* **135**, 16002–16005 (2013).
- 25 Yang, S., Zhi, L., Tang, K., Feng, X., Maier, J. & Müllen, K. Efficient synthesis of heteroatom (N or S)-doped graphene based on ultrathin graphene oxide-porous silica sheets for oxygen reduction reactions. *Adv. Funct. Mater.* **22**, 3634–3640 (2012).
- 26 Ai, W., Luo, Z., Jiang, J., Zhu, J., Du, Z., Fan, Z., Xie, L., Zhang, H., Huang, W. & Yu, T. Nitrogen and sulfur codoped graphene: multifunctional electrode materials for high-performance Li-ion batteries and oxygen reduction reaction. *Adv. Mater.* **26**, 6186–6192 (2014).
- 27 Zhao, Y., Watanabe, K. & Hashimoto, K. Self-supporting oxygen reduction electrocatalysts made from a nitrogen-rich network polymer. *J. Am. Chem. Soc.* **134**, 19528–19531 (2012).

- 28 Silva, R., Voiry, D., Chhowalla, M. & Asefa, T. Efficient metal-free electrocatalysts for oxygen reduction: polyaniline-derived N- and O-doped mesoporous carbons. *J. Am. Chem. Soc.* **135**, 7823–7826 (2013).
- 29 Hou, Y., Wen, Z., Cui, S., Ci, S., Mao, S. & Chen, J. An advanced nitrogen-doped graphene/cobalt-embedded porous carbon polyhedron hybrid for efficient catalysis of oxygen reduction and water splitting. *Adv. Funct. Mater.* **25**, 871–882 (2015).
- 30 Jin, H., Wang, J., Su, D., Wei, Z., Pang, Z. & Wang, Y. In situ cobalt-cobalt oxide/N-doped carbon hybrids as superior bifunctional electrocatalysts for hydrogen and oxygen evolution. *J. Am. Chem. Soc.* **137**, 2688–2694 (2015).
- 31 Liu, Q., Jin, J. & Zhang, J. NiCo₂S₄@graphene as a bifunctional electrocatalyst for oxygen reduction and evolution reactions. *ACS Appl. Mater. Interfaces* **5**, 5002–5008 (2013).
- 32 Masa, J., Xia, W., Sinev, I., Zhao, A., Sun, Z., Grützke, S., Weide, P., Muhler, M. & Schuhmann, W. Mn_xO_y/NC and Co_xO_y/NC nanoparticles embedded in a nitrogen-doped carbon matrix for high-performance bifunctional oxygen electrodes. *Angew. Chem. Int. Ed.* **53**, 8508–8512 (2014).
- 33 Lu, X., Yim, W. L., Suryanto, B. H. R. & Zhao, C. Electrocatalytic oxygen evolution at surface-oxidized multiwall carbon nanotubes. *J. Am. Chem. Soc.* **137**, 2901–2907 (2015).
- 34 Xu, K., Chen, P., Li, X., Tong, Y., Ding, H., Wu, X., Chu, W., Peng, Z., Wu, C. & Xie, Y. Metallic nickel nitride nanosheets realizing enhanced electrochemical water oxidation. *J. Am. Chem. Soc.* **137**, 4119–4125 (2015).
- 35 Mao, S., Wen, Z., Huang, T., Hou, Y. & Chen, J. High-performance bi-functional electrocatalysts of 3D crumpled graphene-cobalt oxide nanohybrids for oxygen reduction and evolution reactions. *Energy Environ. Sci.* **7**, 609–616 (2014).
- 36 Chang, Y., Hong, F., He, C., Zhang, Q. & Liu, J. Nitrogen and sulfur dual-doped non-noble catalyst using fluidic acrylonitrile telomer as precursor for efficient oxygen reduction. *Adv. Mater.* **25**, 4794–4799 (2013).
- 37 Xu, J., Dong, G., Jin, C., Huang, M. & Guan, L. Sulfur and nitrogen co-doped, few-layered graphene oxide as a highly efficient electrocatalyst for the oxygen-reduction reaction. *ChemSusChem* **6**, 493–499 (2013).
- 38 Li, Y., Zhou, W., Wang, H., Xie, L., Liang, Y., Wei, F., Idrobo, J. C., Pennycook, S. J. & Dai, H. An oxygen reduction electrocatalyst based on carbon nanotube-graphene complexes. *Nat. Nanotechnol.* **7**, 394 (2012).
- 39 Ma, T., Dai, S., Jaroniec, M. & Qiao, S. Metal-organic framework derived hybrid Co₃O₄-carbon porous nanowire arrays as reversible oxygen evolution electrodes. *J. Am. Chem. Soc.* **136**, 13925–13931 (2014).
- 40 Man, C., Su, H. Y., Calle-Vallejo, F., Hansen, H. A., Martínez, J. I., Inoglu, N. G., Kitchin, J., Jaramillo, T. F., Nørskov, J. K. & Rossmeisl, J. Universality in oxygen evolution electrocatalysis on oxide surfaces. *ChemCatChem* **3**, 1159–1165 (2011).



This work is licensed under a Creative Commons Attribution 4.0 International License. The images or other third party material in this article are included in the article's Creative Commons license, unless indicated otherwise in the credit line; if the material is not included under the Creative Commons license, users will need to obtain permission from the license holder to reproduce the material. To view a copy of this license, visit <http://creativecommons.org/licenses/by/4.0/>

© The Author(s) 2016

Supplementary Information accompanies the paper on the NPG Asia Materials website (<http://www.nature.com/am>)